ORIGINAL PAPER-PRODUCTION ENGINEERING

Condensation distribution and evolution characteristics of water vapor in annulus of flexible riser

Gangtao Mao[1,2] · Bingliang Zhao[1,3] · Kai Wang[1]

Abstract

Water vapor penetrating an annulus causes condensation and corrosion and endangers the safe operation of the flexible riser. However, in current studies, the condensation of water vapor in the annulus is modeled based on the film condensation hypothesis, which assumes that the metal material is uniformly corroded. This assumption differs from the true corrosion incidents, which are usually initiated by localized corrosion. To further study the condensation law of water vapor in a flexible riser annulus, the evolution of water vapor condensation on the wall surface of a sapphire reactor was evaluated using an annular condensation experimental device. A water vapor condensation growth model was established to analyze the condensation law and its influencing factors. The results show that the maximum radius of condensate droplets on the annular wall surface is approximately 0.48 cm, the average radius of droplets is approximately 0.35 cm, and the volume of condensate that can be accommodated in the 18×18 mm simulation area is approximately 0.5 cm^3. After the droplet reaches the departure radius and falls off a surface, the time of recondensation is faster than that of the first condensation. The condensation surface coverage increases rapidly in the early stage and then gradually slows down. After stabilization, the maximum coverage can reach 80%. Parameter analysis suggests that the number of fixed nucleation points on the condensation wall affects the time to reach the departure radius and the increasing rate of surface coverage. However, the number of fixed nucleation points has minimal influence on the departure radius and coverage outcomes. The findings of this study establish a theoretical foundation for predicting dropwise condensation behaviors in annulus of pipelines and developing corrosion protection strategies that modify the wall contact angle or structure.

Keywords Flexible riser · Annulus · Water vapor · Condensation experiment · Water vapor condensation growth model

List of symbols

Latin letters

A	Area (m^3)
F_n	Surface tension (N)
F_g	Gravity (N)
f	Friction factor
g	Gravitational acceleration (m/s^2)
H	Droplet height (m)
H_{fg}	Latent heat of condensate (J/kg)
$\hat{i}, \hat{j}$	Unit vectors in x and y directions
L	Length (m)
L_{ij}	Distance between two nucleation sites i and j (m)
N	Number
N_f	Nucleation density of droplets on the rough surface (cm^{-2})
N_i	Number of the i-generation droplets
N_s	Nucleation density of droplets (cm^{-2})
n	Droplet distribution index
P	Ratio of the effective area
R	Radius (m)
R_i	Radius of the i-generation droplets (m)
$R_{\min}$	Minimum droplet radius (m)
$R_{\max}$	Critical radius of droplet falling (m)
R_0	Initial nucleation radius of droplets (m)
r	Proportional constant

✉ Kai Wang
   wang_kai@bipt.edu.cn

1   Beijing Institute of Petrochemical Technology, Beijing Key Laboratory of Pipeline Critical Technology and Equipment for Deepwater Oil & Gas Development, Beijing 102617, China

2   School of Energy Resources, China University of Geosciences (Beijing), Beijing 100083, China

3   Beijing Yanshan Company Oil Refinery, China Petroleum & Chemical Corporation, Beijing 102503, China

S	Droplet areas (m^3)
S_i	Surface area covered by the i-generation droplets (m^2)
t	Time (s)
T	Temperature (K)
T_S	Water vapor saturation temperature (K)
ΔT	Undercooling (K)
X	Dimensionless parameter
Y	Dimensionless parameter

Greek letters

β	Proportional constant
φ	Ratio of coverage
σ	Surface tension coefficient (N/m)
ρ	Density (kg/m^3)
ρ_l	Liquid density (kg/m^3)
ρ_v	Vapor density (kg/m^3)
μ	Dynamic viscosity (Pa s)
μ_s	Droplet intrinsic growth index, approximately equal to 0.23
θ	Angle (°)
θ_{adv}	Forward angle (°)
θ_{avg}	Average contact angle (°)
θ_{rcd}	Receding angle (°)

Acronyms

EOS	Equation of state
PVDF	Polyvinylidene difluoride
PA-11	Poly-ω-aminoundecanoyl

Introduction

Research background

Flexible risers, a key tool in offshore oil and gas transportation, have been extensively studied in recent years (Matheus et al. 2020; Wang et al. 2021). Generally, flexible risers are made from multilayer metal strips and barrier materials that are fused through a nonbonding method. A pipe wall is composed of the carcass, internal pressure sheath, metallic layers (e.g., pressure armor and tensile armor), and outer sheath (from inside to outside). Both the internal pressure sheath and the outer sheath are made from polymer materials. The internal pressure sheath is designed to seal the fluid in the bore, and the outer sheath is used to protect the metallic strips from corrosion by seawater. The space between the internal pressure sheath and the outer sheath is defined as the "annulus," in which there is approximately a 5–15% gap between the metal strips. During the oil and gas transportation process, because the polymer material inside the flexible pipeline can be penetrated by gas, small gas molecules inside the pipeline penetrate the annulus through the internal pressure sealing layer; water vapor is a key gas in this

process (Campos et al. 2019; Haahr et al. 2016). Condensation occurs when the pressure of the water vapor in the annulus gradually accumulates to exceed the saturated vapor pressure for the given operating temperature. When vapor accumulates to a certain extent, the pipeline is damaged: if the condensate is not discharged from the pipe sufficiently fast after formation in the annulus, it may result in irrigation. The cooling of the annulus temperature after shutdown could additionally cause the hydrate to block the vent system. Therefore, if the annulus pressure is not discharged in time after reaching the upper limit, the outer protective layer will be broken. Moreover, following condensation, the water vapor penetrating the annulus contacts CO_2, H_2S, and other gases to form an acidic environment and corrode the annulus. When the pressure relief of the inner pipe does not match the annular pressure, it will lead to the collapse of the carcass, which brings hidden dangers to operation of the pipeline. A recent survey completed by Oil & Gas UK reported the failure rate of the metal in the annulus of flexible pipe annuli to be 8.7% based on 384 incidents (MacLeod et al. 2017). This rate is closely related to the permeation and condensation of special gases. Therefore, investigating the condensation behavior of water vapor in the annulus is of vital importance for the safe transportation of oil and gas.

Annular corrosion is an important cause of pipeline failure. At present, annular condensation is the basis for studying the corrosion of metal materials. Many efforts indicate that uniform corrosion occurs on the metal surface in the annulus. The amount of condensation affecting the corrosion rate of CO_2 has previously been analyzed based on the membrane condensation hypothesis (Remita et al. 2008). However, researches in the field of osmotic condensation and phase change-enhanced condensation heat transfer show that the condensate droplets distributed on the inner wall of the flexible riser annulus are distributed in drops that do not flow easily (Wu et al. 2001). The condensation of water vapor in the annulus is in the form of dropwise condensation, and the corresponding corrosion form is local. Compared with uniform corrosion, the droplet thickness in local corrosion exhibits an important impact on the corrosion rate, and this corrosion usually occurs under the condition of a small anode and a large cathode (Tsutsumi et al. 2007; Wang and Kido 2006). In addition, uniform corrosion is calculated by taking the average thickness of all droplets, which ignores the severe corrosion caused by large droplets. This assumption greatly reduces the accuracy of corrosion predictions. Analysis is further complicated by the corrosion speed being particularly fast and the corrosion degree exceeding that predicted by uniform corrosion. These factors make corrosion difficult to predict and detect. In practice, oil and gas pipelines are often replaced due to local corrosion, which leads to pipeline failure (Wang et al. 2020).

Therefore, research on the condensation law of water vapor on annulus metal materials is of great significance to the safe operation of flexible risers. In our previous study, we predicted the total amount of condensation in the annulus by mechanism modeling for the first time (Wang et al. 2021). However, the specific distribution and migration law of condensation is not clear. Therefore, based on previous research, this paper performs a more detailed study of the evolution and distribution of condensate to provide a theoretical basis for corrosion prediction.

Literature review

Research progress in dropwise condensation

There are three main hypotheses of droplet nucleation for the dropwise condensation process, including the membrane rupture hypothesis proposed by Jacob (1936). This hypothesizes that water vapor forms a liquid film on the wall and then ruptures to form droplets. The fixed nucleation center hypothesis proposed by Eucken (1937) suggests that there are many small uneven pits on the wall. These pits are called nucleation points, and when water vapor touches them, a large number of small droplets are formed, merge, and fall off. The third model is the drop-film coexistence hypothesis proposed by Song et al. (1991). They proposed that water vapor simultaneously forms droplets and liquid films on the wall surface. Currently, the fixed nucleation center hypothesis is widely used, which suggests that dropwise condensation is a cyclic process involving nucleation, growth, merging, and shedding of droplets. After shedding, water vapor comes in contact with the exposed new surface and repeats the condensation process.

A more accepted heat transfer model for dropwise condensation was proposed by Rose and Glicksman (1973), which accurately characterizes the heat transfer dynamics of dropwise condensation and agrees with the experimental data of Rose. On this basis, a steady-state formula for calculating droplet size and distribution was proposed (Rose 1981). After, Kim and Kim (2011) developed a mathematical model to analyze the dropwise condensation phenomenon on hydrophobic or superhydrophobic surfaces. Qi et al. (2015) improved the Rose model, developed a fractal dropwise condensation heat transfer model, and analyzed the effect of the contact angle. Zhang et al. (2019) summarized the shortcomings of the previous model and proposed a theoretical framework that treats droplet contact and aggregation as the main mechanisms of size change. In addition, phase-enhanced environmental scanning electron microscopy was also used to observe the dropwise condensation process and to perform statistics on droplet size and distribution (Zhang et al. 2020b).

Research progress in water vapor condensation

Current research on flexible pipelines is limited to structural design and mechanical properties (Amaechi et al. 2022a, b, c; Hu et al. 2021; Liu et al. 2020). A few studies have been performed on the annular water vapor condensation of flexible pipelines based on theoretical models and experiments, discussed as follows.

(1) Theoretical models

Péneloux et al. (1982) corrected the molar volume of water using the volume translation method to improve the prediction of liquid-phase volume. Søreide and Whitson (1992) modified the Peng Robinson equation of state (EOS) to predict the ratio of condensate to steam. Chabab et al. (2019) and Afanasyev and Vedeneeva (2021) improved the above equation to enhance the accuracy of EOS prediction. Based on thermodynamic phase equilibria, Benjelloun-Dabaghi et al. (2002) employed the modified PR equation of state to predict the condensate mass in the annulus.

(2) Experiments

Andersen et al. (1999) investigated water vapor permeation in PVDF and PA-11 using a small test setup and prototype experiments. They calculated the permeability coefficients, which can be used to determine the occurrence of water vapor condensation in the annular space. The tests of both scales proved that the flexible pipeline annulus can be wetted by water vapor when the flexible pipeline conveys the oil and gas mixture. Eriksen and Engelbreth (2014) studied the migration of condensate in a flexible riser annulus for the first time. The results showed that annular conditions change over time as water vapor condensation occurs in the annulus. Condensate forms in some places, while water vapor is present in other places, and the interface between water vapor and condensate is likely to change over time.

The aforementioned tests all confirm that when gas and liquid are mixed, the annulus of the flexible pipeline is wetted by water. When CO_2 and H_2S are contained in the oil–air mixture conveyed in the pipeline, the CO_2 and H_2S acid gases that penetrate the annulus combine with the condensed water to create a corrosive environment. Several studies have investigated the effect of condensate on corrosion. Remita et al. (2008) tested the influence of condensate quality change on the CO_2 corrosion rate for the first time. Taravel-Condat et al. (2003) conducted penetration tests in water containing 3% NaCl at 20 °C and 80 °C and evaluated the influencing factors of the corrosion rate. Clements and

Ethridge (2003) employed existing corrosion data from the literature to fit the corrosion rate and condensate thickness, and their correlation was analyzed.

Research efforts have attributed great importance to the influence of condensation amount on the CO_2 corrosion rate (Islam et al. 2018). However, at present, the corrosion of CO_2 in the flexible pipeline annulus is based on the film condensation hypothesis, which assumes that uniform corrosion occurs on the metal surface in the annulus. The annulus metal corrosion rate is studied according to the ratio of the condensate volume to the material surface area (i.e., liquid film thickness) (Bertoncello et al. 2020; Zhang et al. 2020a, b). Further research on the corrosion of CO_2 in the annulus has suggested that uniform corrosion model based on film condensation is too idealized to capture real-world dynamics. Studies in the field of enhanced condensation heat transfer also show that the possibility of dropwise condensation of water vapor on the annulus wall is greater (Ma et al. 2008; Rausch et al. 2008, 2010). If the water vapor in the annulus is distributed in drops on the wall after condensation, local corrosion occurs on the metal surface (Rozi et al. 2018). The corrosion rate is related to both the acidity and thickness of the drop (Bęben 2021; de Freitas et al. 2021; Vagapov 2021). Thus, actual corrosion is more complicated than uniform corrosion. At present, there are limited studies on condensation in flexible pipeline annuli. It is therefore necessary to further investigate the specific form of condensate distribution and evolution in the annulus.

Study in this paper

According to the current background research, the condensate in the annulus is regarded as film condensation, and the corresponding corrosion is uniform. There is no research on the specific distribution characteristics of vapor droplets in the annulus, such that the results obtained are inconsistent with actual corrosion dynamics. The innovation of this paper is to study the dropwise condensation law and droplet distribution evolution characteristics of water vapor in the annulus of a flexible riser through numerical simulation and full visual experiment, determine the specific distribution and morphological characteristics of the condensate in the annulus, and guide future research of pipeline corrosion. Considering the limitations of previous studies on the condensation law of water vapor in the annulus, an experimental device is designed and built for the water vapor permeation condensation experiment. In addition, the condensation process of water vapor in the annulus is analyzed experimentally. Based on the water vapor condensation mechanism, a water vapor growth model is established and experimentally verified. The condensation behavior of water vapor in the annulus is assessed using measurements of the maximum droplet radius, the average droplet radius, the total volume of condensate, and the surface coverage of condensate.

Due to the limitations of laboratory conditions, it is not possible to use an actual oil–water riser for these experiments. As a result, this paper uses a fully transparent visualized sapphire reactor, which has the characteristics of possessing the same ring structure as the actual annular space and offering full visualization of temperature and pressure resistance. These traits allow for accurate simulation of water vapor condensation processes in the annulus.

Experimental methods

Experimental design

The gas permeation condensation device of the offshore oil and gas flexible riser was designed based on the experimental purpose. As illustrated in Fig. 1, according to the actual structure of the prototype sample tube, the osmotic condensation experimental device is simplified into four components, namely the inner tube, the inner pressure sealing layer, the annulus, and the outer protective layer. The device is constructed using two identical fully transparent sapphire reactors with volume of 400 ml, internal diameter of 80 mm, pressure of 15 MPa, and temperature resistance of -20 to $150\,°C$. Moreover, the inner tube and annulus are equipped with temperature and pressure sensors, which can monitor and record the experimental data in real time. The HD high-speed camera is configured to capture the water vapor condensation process in real-time. The HD high-speed camera has an amplification function, and the magnification is adjustable.

The experimental device is placed in a step-by-step constant temperature chamber. High-temperature water vapor is generated in transparent reactor I, penetrates reactor II through the polymer layer between the upper and lower reactors, and subsequently condenses into liquid water on the transparent glass wall of reactor II. The gas permeation condensation experimental device comprises three key components: the liquid supply system, the permeation condensation system, and the measurement and recording system. The gas supply system can supply one or more gases (e.g., CH_4, CO_2, steam, etc.) simultaneously.

The osmotic condensation system is mainly composed of two fully transparent sapphire reactors I and II, osmotic film placement parts, temperature and pressure sensors, safety valves, vent valves, and heating rods. The measurement and recording system contain a high-definition high-speed camera, electronic display screen, temperature and pressure sensors, data collector, and computer.

Fig. 1 Schematic diagram of the experimental device
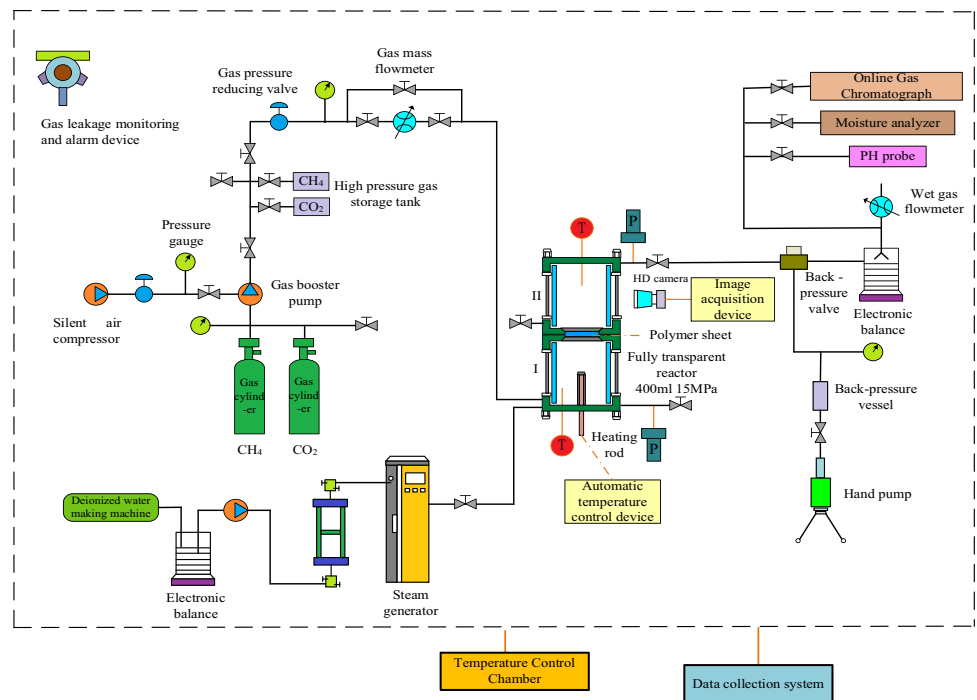
Experimental procedure

(1) The strength and airtightness of the detection device are tested as follows:

① Start the data acquisition software and record various parameters during the experiment;

② Connect the vacuum pump to the venting valve of reactor II to pump the reactors into vacuum;

③ Turn on the deionized water purifier and subsequently turn on the constant pressure and constant flow pump. Pour liquid water into reactor I with sufficient injected water to submerge the heating rod;

④ Turn on the high-definition high-speed camera, connect it to the electronic display, and adjust the magnification and position of the camera until a clear image is captured;

⑤ Use the heating rod to heat the liquid water to produce water vapor, and record the temperature and pressure of the water vapor at this time through the temperature and pressure sensors in reactor I;

⑥ After the water vapor is heated and enters reactor II through the permeable membrane, turn on the video storage function of the high-definition high-speed camera, store the captured water vapor condensation process in the mechanical hard disk, and use the temperature and pressure sensors in reactor II to record the temperature and pressure in the condensation process;

⑦ Repeat experimental steps ③–⑥, and conduct multiple water vapor permeation condensation experiments;

⑧ Record the droplet characteristic data of the above experiment, including the time of the experiment, the temperature and pressure of the gas in reactor I when the gas–liquid two-phase state is formed, the temperature and pressure in reactor II, the conditions when the liquid is formed, the entirety of the water vapor condensation process, etc.

Experimental results

Numerous water vapor condensation experiments were conducted under a vapor temperature of 73 °C, a condensation glass wall temperature of 68 °C, and an undercooling of 5 °C. The selected experimental observation area is 18 mm * 18 mm. The range of the selected area can accommodate the entire process of multi-liquid droplet formation and falling, which shows similar characteristics in other parts of the wall outside this area due to the wall being nearly uniform and having a reliable reference value. It is evident from the extensive experimental data that the condensation mechanism of water vapor on the condensation wall is dropwise condensation. The dropwise condensation of water vapor on the wall can be divided into four stages: nucleation, growth, merging, and falling off. At the initial stage, high-temperature water vapor is generated in reactor I, passes through the permeable film into reactor II, and begins to condense when it encounters the low-temperature glass wall. The penetration of the gas into reactor II through the membrane is a slow process. During the initial nucleation stage, water vapor initially forms a large number of

Fig. 2 Schematic of water vapor primary dropwise condensation

(a) T=120 s

(b) T=349 s

(c) T=1588 s

(d) T=4085 s
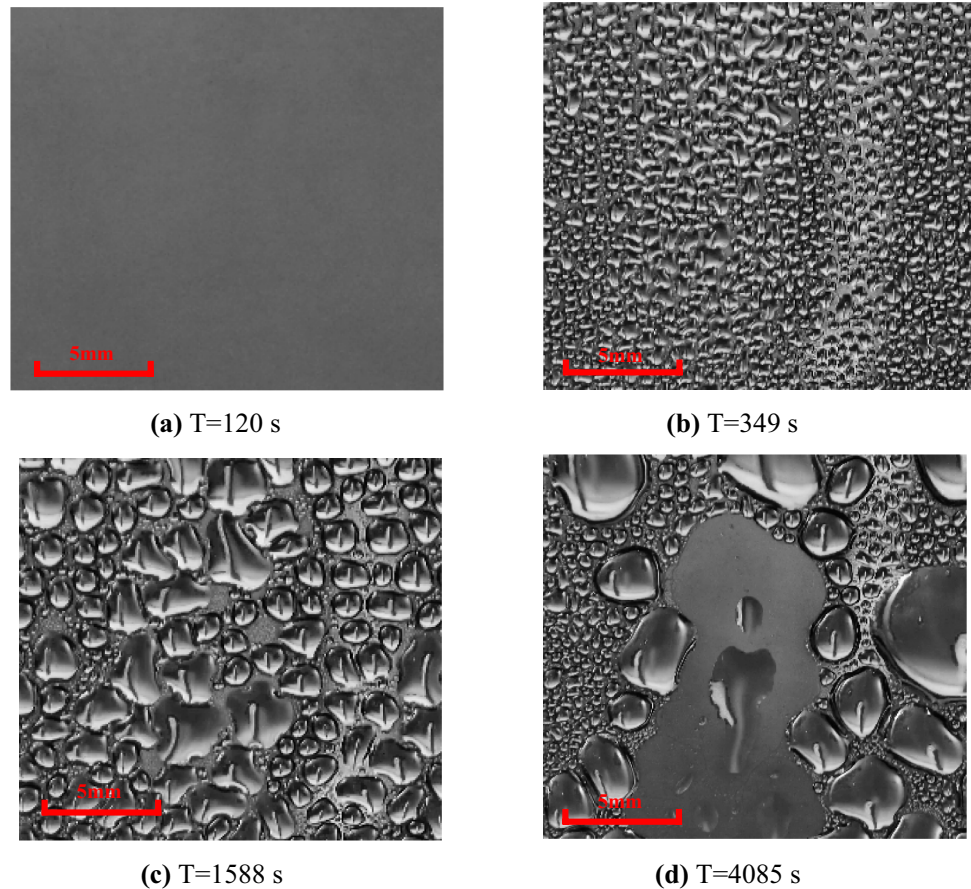
condensation nodules on the condensation wall. As time increases, small droplets at the condensation core begin to absorb the surrounding water vapor and grow, forming a thin mist on the wall (Fig. 2a). During the initial nucleation stage, droplets are randomly distributed on the condensation wall, and each nucleation point has a minimum radius, i.e., the initial nucleation radius. Dropwise condensation requires 5–6 orders of magnitude growth between the initial condensation and the maximum departure radii. During the droplet nucleation and growth stage, the droplet diameter is too small to be photographed by the experimental instrument. After a period of growth, the droplet size gradually increases and grows mainly by direct condensation (Fig. 2b). When the condensate droplets on the wall grow and contact the surrounding droplets, they merge. After merging, the new droplets condense and nucleate on the exposed wall. At this time, the droplets grow mainly by merging (Fig. 2c). Finally, after a growth period, the droplet size gradually increases. When the gravity of the droplet is greater than the surface tension, it will fall off from the condensation wall (Fig. 2d).

After the droplets have completed the entire condensation process of nucleation, growth, merging, and falling off, new condensation nodules are generated at the falling-off point on the wall and repeat the condensation process. Following this, the droplets on the condensation wall enter a dynamic growth stage.

A large number of condensation data on the condensation wall are counted. It is first obtained that the average diameter of the first-generation droplets is 4.915 mm; the average diameter of the second-generation droplets is 3.475 mm; the average diameter of the third generation droplets is 2.240 mm; the average diameter of the fourth generation droplets is 1.602 mm; the average diameter of the fifth generation droplets is 1.097 mm; the radius ratio of two adjacent generations droplets is 1.42; and the number of the first-generation droplets is 2.

According to the effective coverage formula, the effective coverage of droplets on the condensation wall can be calculated as:

$$P = \frac{S_0}{A} \tag{1}$$

where S_0 represents the surface area covered by the first-generation droplets, m^2, and A represents the condensation wall area, m^2.

Effective coverage P is a probability that can only be obtained by statistical analysis of a large number of

experimental data. Therefore, although P cannot be accurately determined from only one set of data, according to the water vapor condensation video, we approximate the diameter ratio of two adjacent generations of droplets. The relationship between P and β can be described as Wu et al. (2001):

$$n = -\lg(1-P)/\lg(\beta) \tag{2}$$

where n is the droplet distribution index, usually 1/3 (Wu et al. 2001), and β is the ratio of the diameters of the two adjacent droplet generations.

When β is equal to 1.42, the calculated P is equal to 0.1103, which is similar to the effective coverage rate of 0.117 calculated by the first-generation droplets. Therefore, the effective coverage of the condensation wall under this working condition is determined to be approximately 0.11.

Under steady-state conditions, the number of droplets in the second to fifth generations of the condensation is approximately 4, 7, 12, and 21, respectively. According to the calculation, the area occupied by each generation of droplets in this range is 34.13 mm^2, 25.33 mm^2, 23.19 mm^2, and 19.84 mm^2, respectively. At this time, the droplet coverage on the condensation surface is approximately 43.33%. Based on the data analysis using ImageJ in Fig. 2a, b, the condensation surface coverage under the experimental conditions is approximately 75.57%. At this time, the theoretically calculated droplet surface coverage is less than the coverage calculated from the actual experimental data. Limited by the accuracy of the experimental camera used, the condensate droplets photographed by the HD high-speed camera only capture the first five generations, and the number of generations and the number of droplets counted somewhat differed with the actual number and quantity of condensation surfaces. Therefore, there is a gap between the theoretical and physically realized results.

Figure 3 shows that the time for the condensate droplets to undergo the entire nucleation, growth, merging, and falling-off processes for the first time is 4085 s. After the droplets fall, the time for the next droplets to undergo the condensation at the exposed condensation core is 2678 s. The longer time for the former can be attributed to the slow rise in the water vapor temperature at the beginning of the condensation stage, wherein the amount of water vapor produced and dissolved in the polymer film is small. This results in a lower mass of water vapor reaching the reactor through the film, and it therefore takes a long time for the condensate droplets on the reactor wall to complete the preliminary condensation process. As time increases, the rate of water vapor generation accelerates and the mass of water vapor dissolved in the polymer film increases.

Simultaneously, the mass of the water vapor permeating through the polymer film into the reactor increased, resulting in a faster growth rate of droplets per unit time. Therefore, the time to complete the condensation growth process of water droplets in the later stage of permeation is shorter than that in the initial stage of permeation.

Numerical simulation

Physical model

The distribution of droplets on the wall after steam condensation is based on the random fractal model, which is constructed as follows:

A square with a unit side length is divided into $n \times n$ equal parts. $P \times n^2$ small squares are chosen randomly. The inscribed circle of the small square is used as the first-generation droplet ($P < 1$) (Fig. 4a). To generate the second-generation droplets, reduce the length to $r \times n$ ($r < 1$), which yields $n/r \times n/r$ small squares with a side length of $r \times n$. Some of these small squares are randomly selected as the second-generation droplets (which cannot be repeated with the first generation) (Fig. 4b), with an effective area ratio P. The effective area ratio is defined as the ratio of the area covered by each generation of droplets to the area not covered by previous generations of droplets. By repeating this process (Fig. 4c, d), a set comprising droplets at smaller scales can be constructed and is denoted as a random fractal model.

Mathematical model

(1) Droplet steady-state mathematical model

Based on the sequential event model of Rose and Glicksman (1973), a steady-state model of droplet distribution is constructed according to three assumptions.

(1) The ratio of the effective area is constant P;

$$P = \frac{S_0}{A} = \frac{S_1}{A - S_0} = \frac{S_2}{A - S_0 - S_1} = \cdots = \frac{S_k}{A - \sum_0^{k-1} S_i} \tag{3}$$

(2) The ratio of the droplet radius of two adjacent generations is constant ($\beta > 1$)β;

(3) The ratio of the area occupied by two adjacent generations of droplets is a fixed value of $1 - P$.

According to rule 2, the relationship between second-generation droplets and first-generation droplets can be obtained as follows:
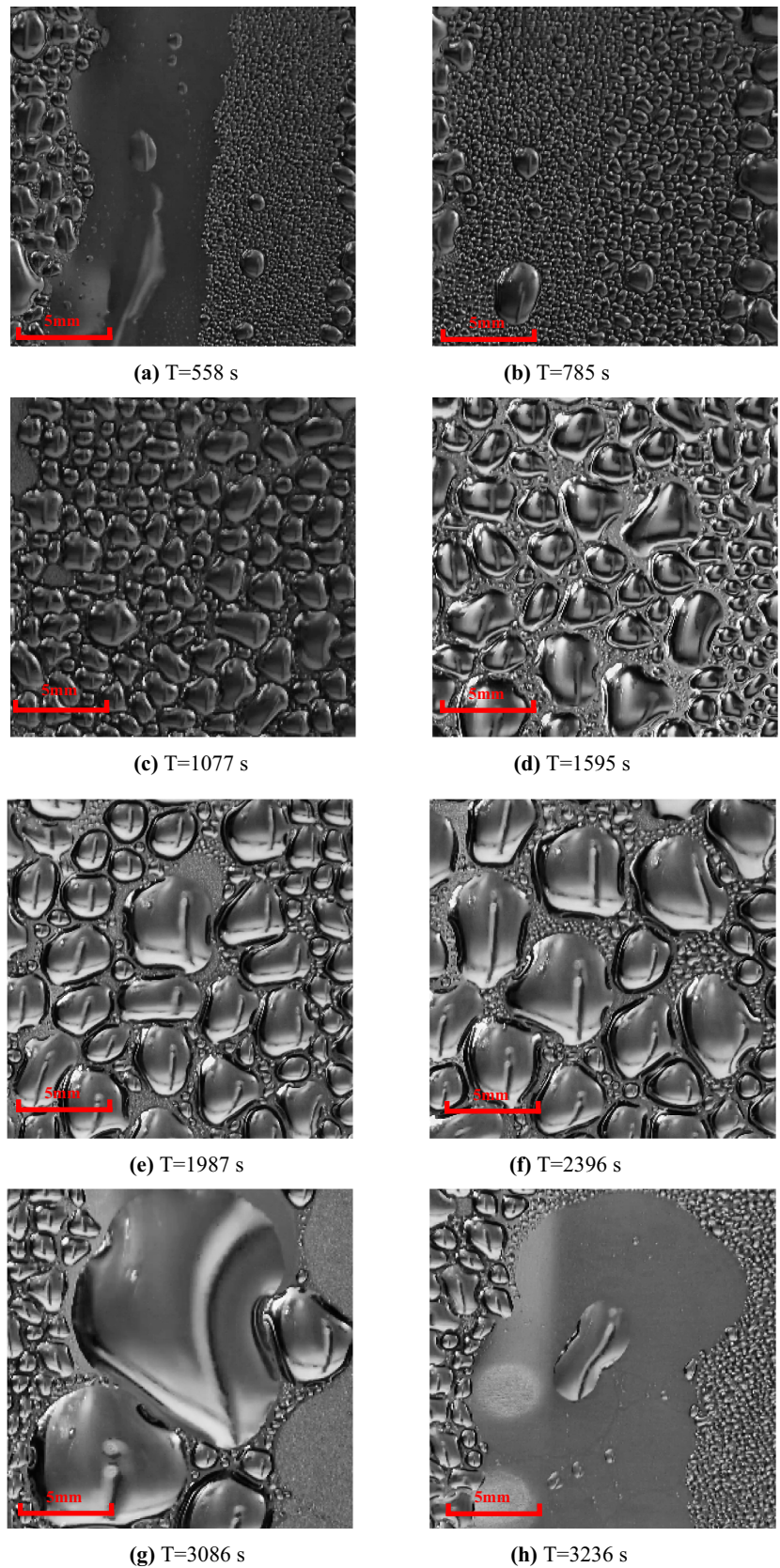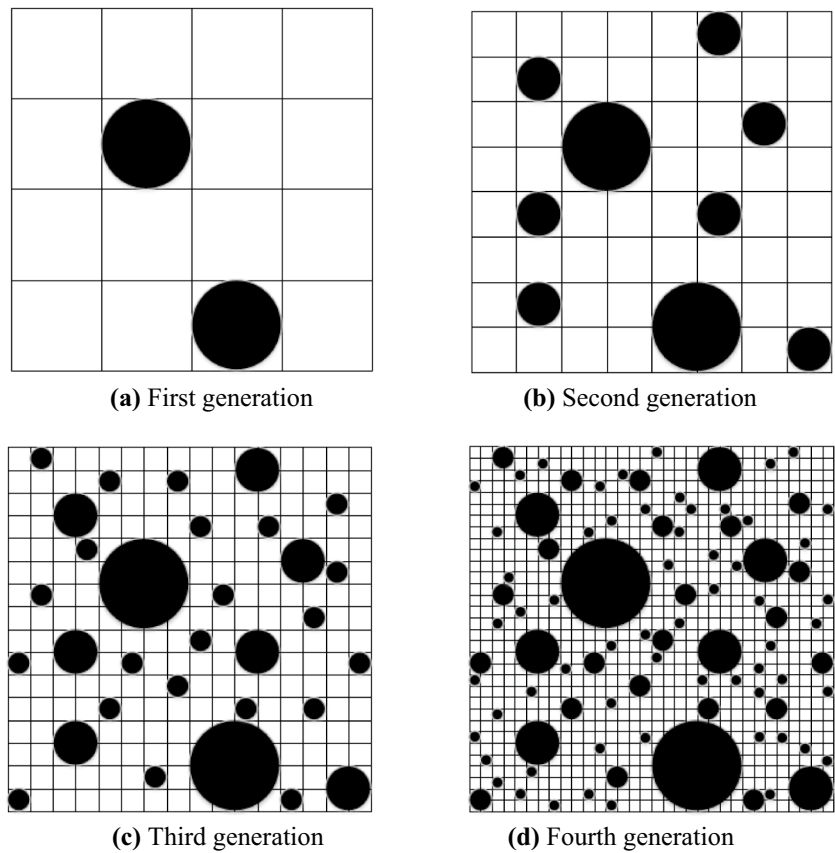
Fig. 3 Schematic of water vapor recondensation

(a) T=558 s

(b) T=785 s

(c) T=1077 s

(d) T=1595 s

(e) T=1987 s

(f) T=2396 s

(g) T=3086 s

(h) T=3236 s

Fig. 4 Random fractal model of droplet distribution

(a) First generation

(b) Second generation

(c) Third generation

(d) Fourth generation

$$R_i = \frac{R_0}{\beta^i} \tag{4}$$

The number of droplets of generation $i + 1$ is then described as:

$$N_i = \frac{S_i}{\pi R_i^2} = N_0((1-P)\beta^2)^i \tag{5}$$

Therefore, the sum of droplet areas of each generation with a radius greater than or equal to R_k is:

$$
\begin{aligned}
S_t(R \geq R_k) &= N_0 \pi R_0^2 + N_0(1-P)\pi R_0^2 + \cdots \cdot N_0(1-P)^k \pi R_0^2 \\
&= N_0 \pi R_0^2 \frac{1 - (1-P^{k+1})}{P}
\end{aligned}
\tag{6}
$$

The sum of the number of droplets of each generation with a radius greater than or equal to R_k is:

$$
\begin{aligned}
N_t(R \geq R_k) &= N_1 + N_2 + \cdots + N_k \\
&= N_0 + N_0(1-P)\beta^2 + N_0(1-P)^2\beta^4 \\
&\quad + \cdots + N_0(1-P)^k\beta^{2k} \\
&= N_0 \frac{((1-P)\beta^2)^{k+1}}{(1-P)\beta^2 - 1}
\end{aligned}
\tag{7}
$$

The droplet surface coverage after a steady state is:

$$\varphi = \frac{S_t}{A} \tag{8}$$

(2) Macroscopic mathematical model of droplets

At the macroscale, droplet condensation is the result of time-related subprocesses. These processes are a function of the formation of droplets at the nucleation position, the direct condensation growth of droplets on the wall, the combined growth, the falling off of droplets under the action of gravity, and the recondensation growth at the exposed fixed nucleation point. Mathematical models of these subprocesses are needed to describe the entire dropwise condensation process as follows.

(1) Initial nucleation radius

The first step in the condensation growth of water vapor on a wall is to fix nucleation on the condensing wall surface. N_0 locations on the surface of unit edge length are randomly selected as random nucleation with a given initial nucleation radius. Since the initial droplet size of water vapor is very small, e.g., in the micro nanometer scale, it is difficult to determine the droplet nucleation radius experimentally.

Khandekar and Muralidhar (2014) described the initial droplet nucleation radius through theoretical derivation:

$$R_{\min} = \frac{2T_S\sigma}{H_{fg}\rho} \frac{1}{\Delta T} \tag{9}$$

where T_S is the water vapor saturation temperature, K; σ is the surface tension coefficient, N/m; H_{fg} is the latent heat of condensate, J/kg; and ΔT is the undercooling, K.

(2) Nucleation density

When the fluid condenses on the wall, the initial condensate droplet radius is approximately a few nanometers, making it difficult to experimentally capture the initial nucleation of droplets on the condensation wall. Therefore, the experimental determination of droplet density on a condensation wall has proven to be complex. Leach et al. (2006) showed that the initial nucleation density of droplets is 10^6 cm^{-2} when the temperature difference is 50–100 °C. For the condensation of water at 30 °C, the initial nucleation density can gradually increase from 10^4–10^5 cm^{-2} to 10^6 cm^{-2}. Rose (2002) proposed the following formula to calculate the nucleation density of droplets:

$$N_S = 0.037/R_{\min}^2 \tag{10}$$

where $R_{\min}$ is the minimum droplet radius, m.

Mu et al. (2008) found that the nucleation density varies with the surface morphology, and coarser planes increase the nucleation density. The nucleation density is affected by the degree of surface morphology and the temperature difference (Rose 2002; Mu et al. 2008). The corrected nucleation density is described as:

$$N_f = f \cdot N_S \tag{11}$$

where N_f is the nucleation density of droplets on the rough surface and f is the friction factor.

(3) Direct condensation growth

In the second stage of water vapor growth, the droplet size becomes relatively uniform, and the droplet distribution is dense. The droplet radius varies with growth time and follows a power exponential relationship. At this time, the droplets do not merge and instead grow mainly by absorbing the surrounding water vapor. The relationship between droplet radius and time is as follows:

$$R = R_0 \cdot t^{\mu_s} \tag{12}$$

where μ_s is the droplet intrinsic growth index, approximately equal to 0.23, and R_0 is the initial nucleation radius, m.

(4) Droplet coalescence

Merging occurs when the droplets grow and come into contact with surrounding droplets. At this time, the droplets on the condensed surface grow mainly by merging with the surrounding small droplets. Based on relevant experimental observations, a simple droplet polymerization model is used here. The center of gravity of the merged new droplets is located at the center of mass of the two droplets.

The distance between any two nucleation points is:

$$L_{ij} = \sqrt{\left(x_i - x_j\right)^2 + \left(y_i - y_j\right)^2} \tag{13}$$

and the critical conditions for consolidation are:

$$L_{ij} - \left|R_i - R_j\right| < 10^{-6} \tag{14}$$

The polymerization process of droplets does not consider the influence of polymerization time. As soon as the droplets come into contact with each other, they are replaced by a single droplet with the same total volume as the two droplets. The coordinates of the new droplet after the merger are related to the prior coordinates of the two droplets. According to the mass conservation law, the radius of the merged droplets is:

$$R_3 = \sqrt[3]{R_1^3 + R_2^3} \tag{15}$$

The coordinates of the merged droplets are:

$$x_3 = \frac{x_1 R_1^3 + x_2 R_2^3}{R_1^3 + R_2^3} \quad y_3 = \frac{y_1 R_1^3 + y_2 R_2^3}{R_1^3 + R_2^3} \tag{16}$$

The droplet height is:

$$H = R \cdot \text{tg}\left(\left(\theta_{adv} + \theta_{rcd}\right)/2\right) \tag{17}$$

where θ_{adv} is the forward angle, °, and θ_{rcd} is the receding angle, °.

(5) Droplet slip

The effective slip radius is estimated by the force balance between surface tension and gravity. The surface tension of a droplet perpendicular to an inclined wall is:

$$F_n = \pi\sigma R\left(\sin\theta_{adv} + \sin\theta_{rcd}\right) \tag{18}$$

The gravity component perpendicular to the inclined wall is:

$$F_g = \frac{\pi R^3 \left(2 - 3\cos\theta_{avg} + \cos^3\theta_{avg}\right)}{3\sin^3\theta_{avg}}(\rho_l - \rho_v)g\cos\theta \quad (19)$$

where θ_{avg} is the average contact angle, ρ_l is the liquid density, kg/m^3, and ρ_v is the vapor density, kg/m^3.

When gravity and surface tension are balanced, the critical radius of droplet falling is:

$$R_{max} = \frac{3\sin\theta_{avg}\left(\sin\theta_{adv} + \sin\theta_{rcd}\right)}{\left(2 - 3\cos\theta_{avg} + \cos^3\theta_{avg}\right)}\left(\frac{\sigma}{g\cos\sigma\left(\rho_l - \rho_v\right)}\right) \quad (20)$$

Independent check of grids and time steps

The calculation area for the numerical simulation in this paper is 18 mm * 18 mm, which is consistent with the size of the picture taken by the HD camera in the experiment. This corresponds to intercepting a small portion of the annular wall of the flexible riser for numerical simulation. Moreover, due to the small calculation area, the intercepted annulus surface can be approximated as a flat area. In this region, the two processes of initial condensation and the recondensation of water vapor on the annulus wall are simulated. The initial droplet diameter is 1.147×10^{-4} cm, and the droplet departure radius is 0.4459 cm. The liquid surface tension is 0.06482 N/m. Furthermore, the liquid density is 1000 kg/m^3, the vapor density is 0.6433 kg/m^3, the vapor saturation temperature is 73 °C, and the wall temperature is 68 °C.

The condensation of the water vapor on the annulus wall was evaluated in MATLAB. The independence of the time step and the number of grids is calculated according to the above model with an appropriate time step size and number of grids selected. Figure 5a shows the variation curve of the maximum droplet radius with time steps of 1, 3, 5, 7, and 9 s. At time steps of 1 s, 3 s, and 5 s, the time for the droplet to reach the departure radius is the shortest, and the three droplets almost coincide. As the time step continues to increase, the time to reach the departure radius at 7 s and 9 s also increases. The two-dimensional calculation area is divided into 3.6×10^5, 6.4×10^5, and 8.1×10^5 grids, and the spacing of each grid node is 3×10^{-2} mm, 2.25×10^{-2} mm, and 2×10^{-2} mm, respectively.

Under these three sets of grid conditions, the influence of the number of grids on time was verified when the number of fixed nucleation points was 1000 (Fig. 5b). The number of grids is 3.6×10^5 in the calculation example. The time for condensate droplets to reach the departure radius is larger than that of the other two groups, and the time from the beginning of droplet growth to the first critical radius is very close in the 6.4×10^5 and 8.1×10^5 grid cases. Therefore, to improve the simulation accuracy and reduce the calculation time, the time step and number of grids for the simulations were set as 5 s and 6.4×10^5, respectively.

Validation

The condensation of water vapor on the wall of the flexible riser is composed of four key processes: fixed nucleation, direct growth, combined growth, and droplet sliding. Figure 6 shows the experimental and simulated areas, both with an area size of 18 mm * 18 mm. Comparative images of the time-varying process of the initial condensation of droplets were taken and simulated. Figure 6a–d shows images of
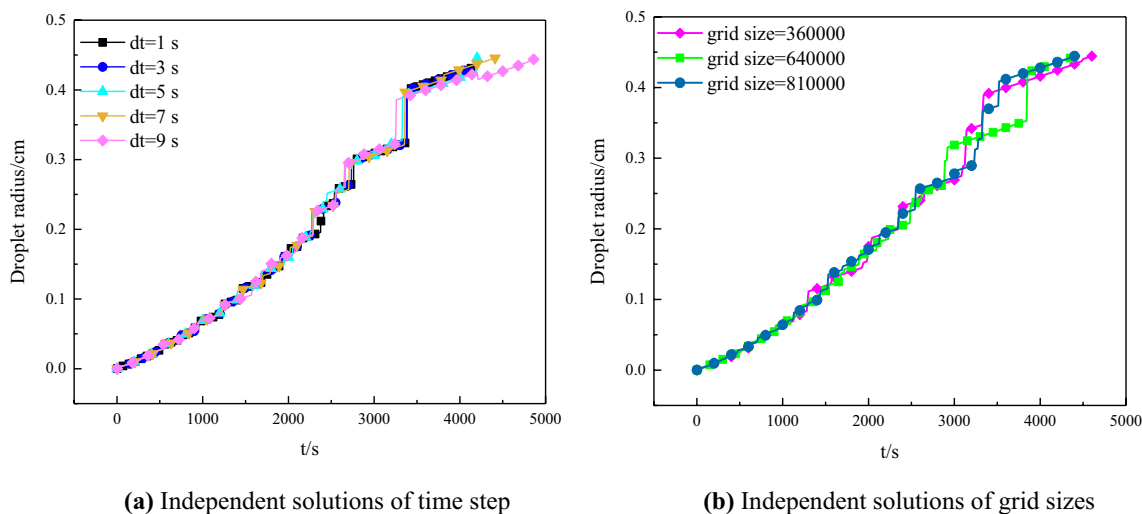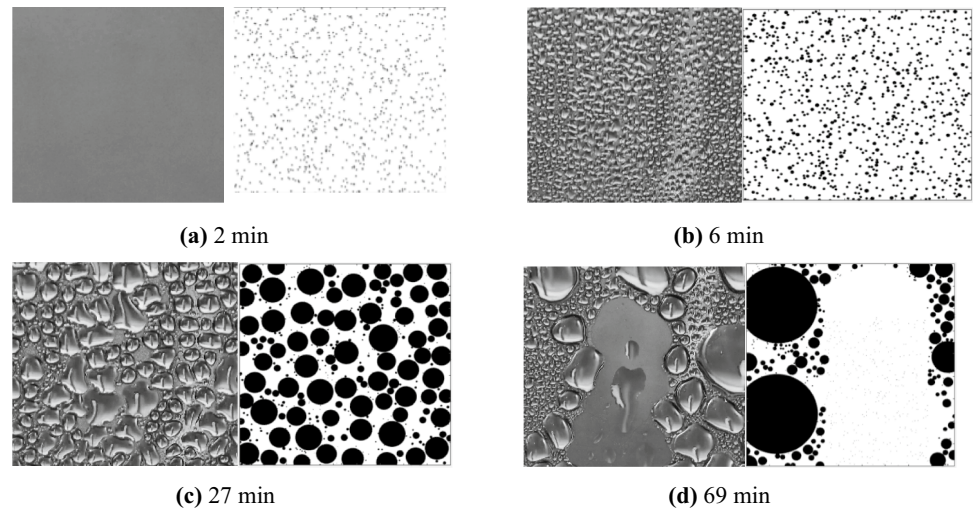

(a) Independent solutions of time step

(b) Independent solutions of grid sizes

Fig. 5 Changes in droplet radius under different time steps and grid sizes

Fig. 6 Experimental and numerical droplet initial condensation process

(a) 2 min

(b) 6 min

(c) 27 min

(d) 69 min

nucleation, growth, merging, and falling off during the vapor condensation process. The condensation of water vapor on the wall is observed as dropwise condensation. The water vapor is first fixed and nucleated on the wall, with each nucleation point having the minimum radius (Fig. 6a). Over time, the fixed nucleation point begins to grow by absorbing water vapor from the surrounding area (Fig. 6b). When the droplets grow to a certain scale, they contact and merge with neighboring droplets (Fig. 6c). When these droplets grow gradually and reach the critical radius, they fall off from the condensation wall (Fig. 6d).

Comparing the spatial and scale distribution of droplets on the condensation wall at different times in the four processes of water vapor dropwise condensation shows that the numerical simulation images in Fig. 6a–c are generally consistent with the droplet distributions in the experiment. When the droplets gradually grow to the critical radius, the droplets fall off from the condensation wall and sweep all droplets in the sliding region, as shown in the experimental and simulated images in Fig. 6d. In particular, there is a deviation between the position of the droplet falling-off point and the number of large droplets left on the condensation

Fig. 7 Experimental and numerical recondensation process after droplet slip

(a) Slip

(b) Nucleation

(c) Grow

(d) Merge

(e) Slide down again
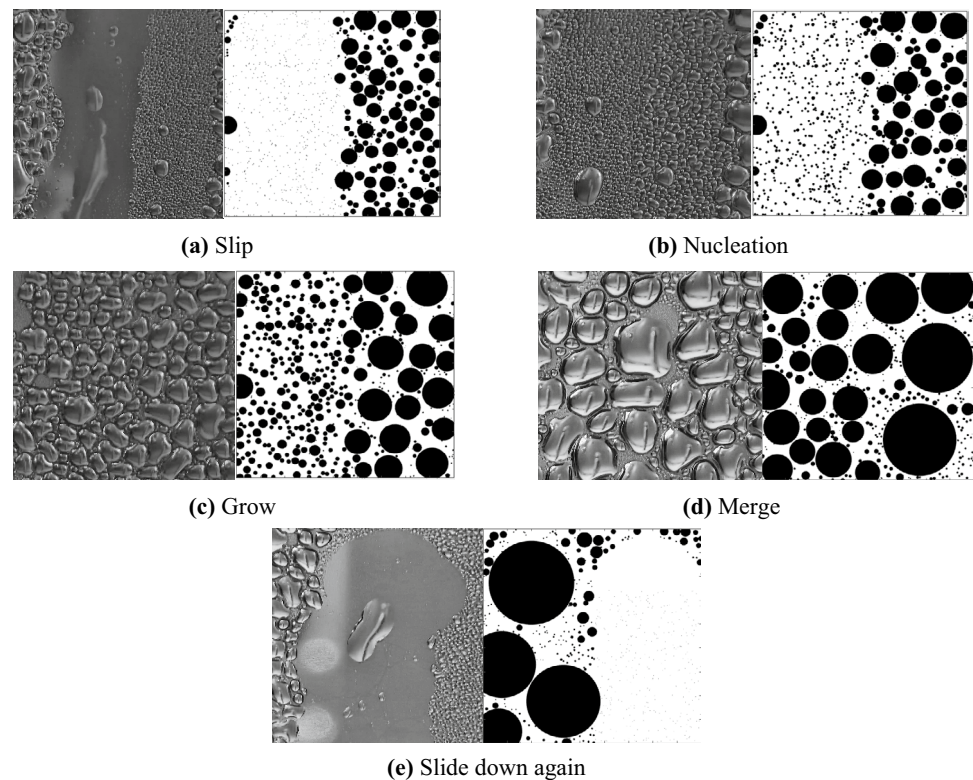
wall after falling off. This can be attributed to the random position distribution of the initial nucleation points on the condensation wall in the experiment. Thus, it is unlikely that the coordinates of all fixed nucleation points in the numerical simulation are completely consistent with the fixed nucleation coordinates of the droplets in the experiment. Although this leads to deviations between the backward images of large droplet removal during the final droplet growth process and the experimental images, the model is still in relatively good agreement with the experiment. Therefore, the errors in these results are considered to be within a reasonable range.

Figure 7a shows an image of the droplet falling from the condensation wall. As the droplet reaches the departure radius, it removes all the droplets along the path. The water vapor then recondenses in the falling region and undergoes the four-growth cycle of droplet nucleation, growth, merging, and falling (Fig. 7b–e). As the droplets on the left side of the condensation wall recondense and nucleate, the droplets on the right side grow. Therefore, the droplet size on the right side of the condensation wall is always larger than that on the left side during the growth process. In addition, the droplets on the right side fall off first. The overall simulation image of the droplet recondensation process is in favorable agreement with the experimental image. Thus, the feasibility of the proposed numerical simulation method is verified by the simulation and experimental results of the initial condensation of droplets and the recondensation after droplet sliding.

Discussion

This section analyzes the trends of the maximum droplet radius, the average droplet radius, the total volume of condensate, and surface coverage with time under different fixed nucleation numbers during the dropwise condensation process.

During the dropwise condensation growth process, 1000, 2000, 3000, 4000, and 5000 fixed nucleation points were selected to investigate the effect of the different numbers of fixed nucleation points on the time to first reach the maximum departure radius. The 6.4×10^5 grids are numbered to ensure that the change in the location distribution of nucleation points would not affect the simulation results when the fixed nucleation point locations were selected. The grid numbers are randomly sorted using the random function rand perm in MATLAB, and the first 1000, 2000, 3000, 4000, and 5000 points are taken out from the arranged grid numbers in turn. In this way, the later fixed nucleation points in the simulation are increased sequentially on the basis of the previous nucleation points, which ensures that the positions of the fixed nucleation points are both random
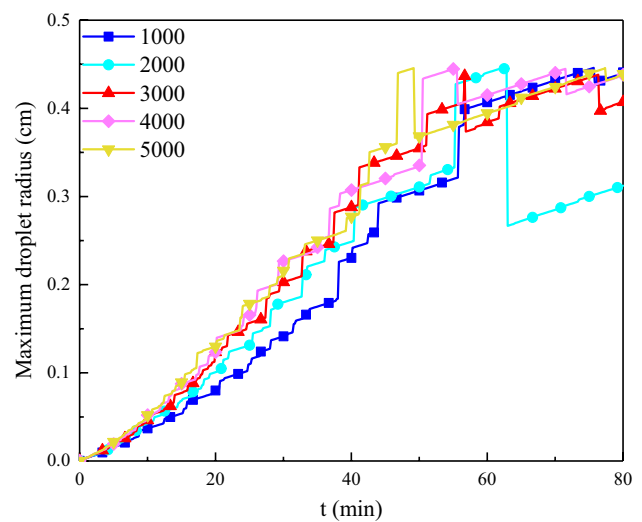

Fig. 8 Change in droplet maximum radius with time under different fixed nucleation sites

and identical, and the influence of the different distribution of nucleation points on the numerical simulation results is reduced. Moreover, considering the influence of the fixed number of nucleation points on the computational efficiency, the maximum number of fixed nucleation points is set as 5000.

Maximum droplet radius

Figure 8 shows the variation in the maximum droplet radius with time for different numbers of fixed nucleation points. The maximum radius of droplets increases with time in the five curves. The time for droplets to reach the departure radius decreases gradually with the increase in the number of fixed nucleation points. The examples of 5000, 4000, 3000, 2000, and 1000 fixed nucleation points with the corresponding times to reach the departure radius are 49, 54, 57, 63, and 75 min, respectively. However, when the number of droplets increases, the process of continuing to increase the number of fixed nucleation points has little effect on the time required for the droplets to reach the departure radius. This occurs because when the number of fixed nucleation points increases, the droplet density increases, which leads to an increase in the droplet merging probability and reduces the time for droplets to reach the abscission radius. After the fixed nucleation points increase sufficiently, the droplet density corresponding to the minimum nucleation radius reaches a limit, and there are no more positions at which to generate droplets and increase the probability of merging. Thus, the time to reach the departure radius stabilizes. We further describe this process according to the following stages.

The maximum radius of droplets with 1000–5000 fixed nucleation points increases at the same rate over time during the first 10 min of droplet growth. This indicates that the droplets on the condensation wall grow mainly by absorbing the surrounding water vapor. No coalescence occurs between the droplets. After 10 min, there is a gap between the maximum radius of 1000 fixed nucleation points and the other fixed nucleation points. Therefore, in the case of more than 1000 fixed nucleation points, droplets started to merge after 10 min. The maximum droplet radius for each number of fixed nucleation points increases at a steady rate from 10 to 38 min. After 38 min, the maximum radius of droplets increases both steadily and in steps. This occurs because although droplets merged and grew on the walls of different fixed nucleation points after 10 min, the radius of droplets on the condensation wall before 38 min is small and does not vary much, so the increase in droplet radius is stable after merging occurred. Over time, small droplets are gradually merge into the large droplets, and the radius difference between different droplets begins to increase. When large droplets and small droplets merge, the radius of large droplets increases, but because the small droplets contribute a small portion of the resulting volume, the influence on the radius of large droplets is minimal and shows a stable growth trend. When large droplets merge with droplets with a small difference in size, the influence on the increase in the radius of the merged droplets is greater, so there is a sudden stepwise increase in the radius of droplets.

When the droplet reaches the maximum departure radius, it slides down the condensation wall and take all the droplets on its path with it. As a result, the maximum radius of the droplet suddenly decreases. The sudden drop in maximum droplet radius is shown (Fig. 8). When the large droplet slips off, the remaining droplets continue to grow, and the maximum droplet curve does not drop to zero. Thus, there are the sudden decrease and subsequent rise in the maximum droplet radius curve.

Average droplet radius

Figure 9 presents the variation in the average droplet radius on the condensation wall over time for different numbers of fixed nucleation points. During the entire droplet condensation growth process, the average droplet radius initially increases, then decreases, returns to increasing, and finally decreases. The degree of difference between the growth trend of the 1000 fixed nucleation points and that of other fixed nucleation points in the same growth time is similar to that in Fig. 8. According to the analysis of the average radius change of 1000–5000 fixed nucleation points, the average droplet radius during the whole growth process in the late condensation period is 0.20–0.35 cm range. The drop average radius decreases differently during the growth time after the droplet falls off until the maximum departure radius is reached again. This is because the droplet radii at different locations on the condensation wall vary in size and are not distributed regularly. Thus, the droplets on the path after large droplet shedding have a random nature, and the decrease in the average droplet radius for each large droplet shedding occurs at different fixed nucleation sites which is different but still within the range of 0.20–0.30 cm. The number of fixed nucleation points shows little impact on the average radius of the droplet sliding down and only affects the time when the droplet reaches the departure radius.
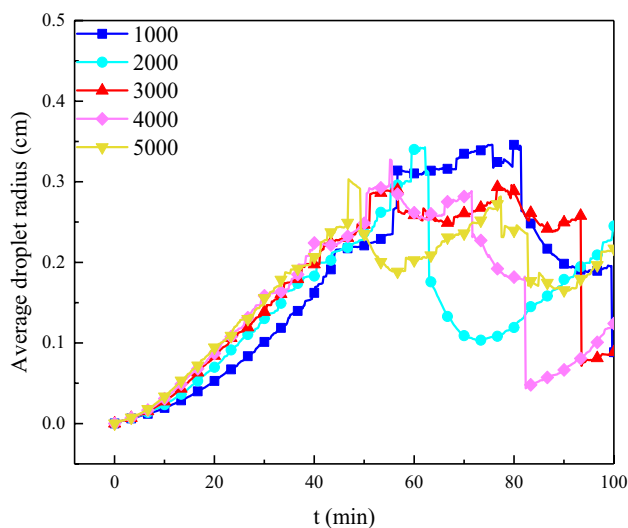

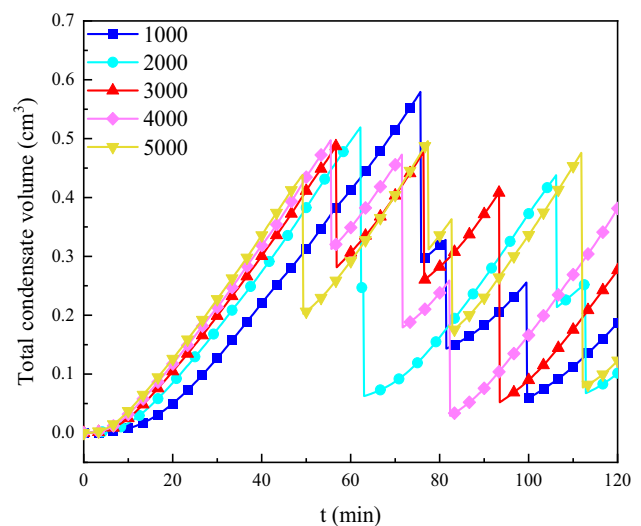**Fig. 9** Change in droplet average radius with time under different fixed nucleation sites

Fig. 10 Change in the total volume of condensate with time under different fixed nucleation sites

Total condensate volume

Figure 10 shows the change in total condensate volume with time at different fixed nucleation points in the simulation domain. The trend of the curve shows that the total condensate volume gradually increases with time, and the wall with the largest number of fixed nucleation points reaches the maximum condensate volume first. When the largest droplet falls off, the total volume of the condensate on the wall drops suddenly, and the remaining droplets continue to absorb the surrounding water vapor or grow by merging the surrounding droplets. Thus, the total liquid volume curve decreases suddenly and then continues to rise. The maximum volume of condensate that can be accommodated on the wall fluctuates by approximately 0.5 cm^3.

Comparing the curves of different nucleation points shows that the higher the number of fixed nucleation points, the lower the maximum volume of condensate in the initial condensation. This occurs due to the high density of droplets distributed on the wall when the droplets on the condensation wall with many initial fixed nucleation points start to grow. Hence, the total volume of condensate on the wall with high nucleation density is higher than that of the other wall condensates with low nucleation density in the early stage. Over time, the number of droplets on the wall with high nucleation density grows to be relatively large, and the probability of collision between adjacent droplets is greater. This results in droplets with high nucleation density reaching the departure radius faster. Because the falling droplets take all the droplets on the sliding path at the same time, which results in the need for small droplets to be carried away before they reach their maximum volume, the total condensate volume on the wall with high nucleation density is the lowest when the droplets fall for the first time. In addition, the reduction in the total volume of condensate on the wall is inconsistent when large droplets fall off since it is impossible to determine the position of the falling droplets and the total volume of the droplets on the falling path when the droplets fall. For example, the total volume of the droplets on the wall with 2000 fixed nucleation points exhibits the greatest decrease after the first slide, and the total volume of the droplets on the wall with 4000 fixed nucleation points exhibits the minimum decrease after the first slide. The reasons for the difference in the curves drop after the droplet slides are shown to be similar. Simultaneously, the total volume of condensate on the walls of the different fixed nucleation points was inconsistent except for the sliding droplet when the droplet reached the shedding radius again, such that the total volume of condensate on the different condensation walls fluctuated greatly each time the droplet slid off. However, a comparison of the total volume curves of condensate on the walls of the different fixed nucleation points showed that the maximum volume of condensate on
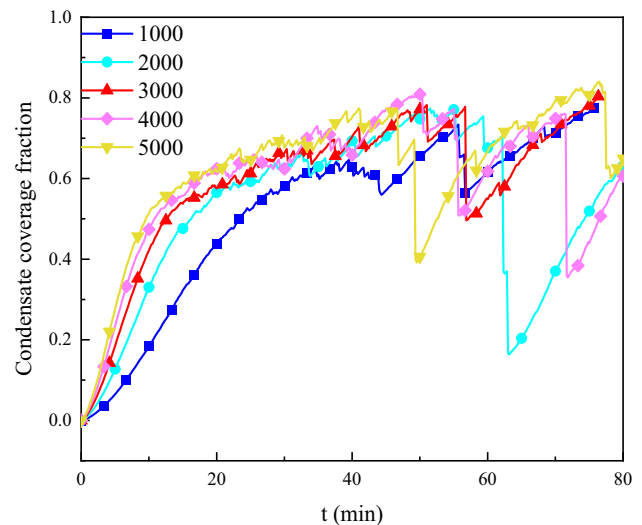

Fig. 11 Change in condensation surface coverage with time under different fixed nucleation sites

the walls fluctuated approximately 0.5 cm^3, so the maximum volume of condensate that could be accommodated on the walls was considered to be approximately 0.5 cm^3.

From these data, it can be concluded that the number of fixed nucleation points has little effect on the rising rate of the total condensate volume and greatly impacts the fluctuation of the total condensate volume when the droplets on the wall slide down. A comparison of the total volume curves of condensate on the wall with different fixed nucleation points reveals that the maximum volume of condensate on the wall fluctuates by approximately 0.5 cm^3.

Condensate surface coverage

Figure 11 presents the variations in condensate surface coverage on the surface with time for different fixed nucleation point numbers on the condensation wall under the same growth conditions. The more fixed nucleation points there are, the shorter the time for the wall to reach the maximum condensate surface coverage, but the number of fixed nucleation points on the condensation wall has little effect on the droplet coverage, which fluctuates by approximately 80%. This process can be divided into the following stages.

First, as the time increases, the condensate surface coverage exhibits the fastest increase from 0 to 20 min. After 20 min, the growth trend of the condensing surface coverage slows down and eventually stabilizes. This is because in the initial stage, the droplet grows mainly by absorbing the surrounding water vapor. Due to its small radius, simultaneously absorbing the same amount of water vapor exhibits a great impact on increasing the droplet radius. This results in a rapid growth trend for condensate coverage. In the later stage of condensation, the droplets continue to grow, and

the number of droplets with larger radii begins to increase. Although the absorption and combination of small droplets also contribute to the increase in large droplet volume, they are insignificant compared to the entire large liquid volume. Thus, its contribution to the increasing large droplet radius is limited, and the increasing trend of condensate surface coverage slows down during the later stage.

After, when the droplet is about to reach the maximum condensate coverage, the curves suddenly decrease and then continue to increase. This occurs because at this time, large droplets merge, the old droplets disappear, and new large droplets form. Although the volume of the large droplets is equal to the volume of the two old droplets, the surface area occupied by the new droplets is smaller than that occupied by the previous two droplets, resulting in the above phenomenon. When the condensate coverage decreases and increases again, the rate of increase is greater than the growth rate recorded before the condensate coverage decreased. This is attributed to the formation of new droplets. After the old droplets disappear, the wall is exposed and new fixed nucleation points are formed on the exposed regions. Due to its small volume, the exposed wall absorbs water vapor of the same size, resulting in a faster increase in the condensate droplet radius, and small droplets occupy the surface area at a greater rate. Following this, the increasing trend of total condensate coverage slightly accelerates.

Practical application of the model

In recent years, high-tech fields such as microelectronics have developed rapidly, and microscopic heat transfer problems within these fields have received greater attention. Dropwise condensation is the most ideal way to strengthen heat transfer. If the method can be applied to change the wetting properties of the surface so that film condensation can be converted to dropwise condensation, then without traditional processing technology, heat transfer can be strengthened, which is of great significance for saving raw materials, energy consumption, and engineering costs. Therefore, maintaining dropwise condensation on the surface of materials commonly used in engineering technology for a long time has become a hot research topic in recent years.

By establishing the droplet growth model and heat transfer model, the influencing factors of droplet condensation growth are analyzed to provide theoretical guidance for the optimal design of micro- and nanostructured surfaces. For water vapor condensation in the annular space, a theoretical model based on the study in this paper can be established to analyze the behavior and process of water vapor condensation, and the factors influencing water vapor condensation can be quantified in terms of contact angle and subcooling, thus providing a

theoretical basis for the modification of the annular space walls on site (e.g., adding protective coatings to change the wettability and electric heating to change the internal temperature).

Limitations and outlook

Due to the limitation of experimental materials and funds, it is difficult to directly take offshore risers for the test. Combined with the needs of the experiment, we carried out the condensation experiment in a temperature- and pressure-resistant sapphire reactor. At the beginning of the experiment, an iron sheet was placed in the reactor to observe the corrosion. However, since the outer layer of sapphire adsorbs water droplets, the HD camera was not able to observe these droplets attached to the iron sheet. Therefore, the condensation behaviors of droplets on the wall can be observed directly without adding other materials. The roughness, surface morphology, and interfacial tension of water between the iron sheet and the sapphire kettle are different, and the condensation state of the droplets is somewhat affected. However, due to the slow penetration rate of steam, the mass of droplets condensed on the wall is small. In addition, the sapphire reactor is an annular vertical space, which is closer to the shape of the marine flexible riser. Therefore, a sapphire reactor can be used for approximate simulation. Moreover, this study highlights the difference between dropwise condensation corrosion and the conventional uniform corrosion (with the latter being the focus of most literature). Therefore, this paper only offers a preliminary qualitative study of the droplet condensation behavior in the annular space. The effects of droplet condensation in the actual annulus and surface morphology temperature on droplet condensation need to be further studied. In addition, the effect of the droplet distribution and thickness on the corrosion rate is only in the qualitative stage, and more work is required to guide the anti-corrosion process. The quantitative effect of droplet thickness on the corrosion rate of annular metal materials will be the focus of future research.

To further study the annular condensation of marine flexible risers, we plan to design a more practical experimental. At present, this work is in its early stages. The new experimental device can more accurately study the influence of surface topography and temperature on droplet condensation from a quantitative point of view and explore its influence on corrosion. We will further study the gas condensation behavior in the annulus in future.

Conclusions

In this paper, an innovative experimental apparatus for annular dropwise condensation using a fully visualized sapphire reactor has been built. A theoretical model of

dropwise condensation has been proposed accordingly. The dropwise condensation process in an annulus of a flexible riser has been analyzed. The influencing factors of water vapor condensation were investigated by numerical simulations utilizing a self-developed MATLAB program. The following conclusions are obtained:

(1) The effective coverage of droplets during the entire dropwise condensation process for each generation was calculated to be approximately 0.11, and the ratio of radii of adjacent-generation droplets was approximately 1.42. When the droplets reach their critical radius and fall off, the time required to complete the condensation process again is shorter than that of the first condensation process. The average radius of condensate droplets on the annular wall surface is approximately 0.35 cm, and the maximum radius is 0.48 cm. After stabilization, the maximum condensate coverage can reach 75.57%.

(2) Combining the simulation results of the water vapor condensation model with experimental data shows that water vapor condensation in the annular space is described by four processes: fixed nucleation, direct growth, combined growth, and droplet slip. Additionally, upon comparing the droplet distribution and condensate coverage, a significant similarity between the predicted and experimental results is observed, which provides support for the accuracy of the model.

(3) The number of fixed nucleation sites on the condensation wall affects the droplet radius and the condensate surface coverage on the wall. A greater number of fixed nucleation sites lead to a shorter time for droplets to attain descent radius, a smaller total volume of condensate at each droplet slip, and a reduced time to achieve maximum surface coverage.

(4) The roughness of the flexible riser annulus wall surface and the number of fixed nucleation points influence the distribution of condensate droplets and thus the corrosion of the annulus metal material. The results provide a theoretical basis for the development of corrosion protection strategies that change the wall contact angle or structure, but the quantitative effect of droplet thickness on the corrosion rate of annular hollow metal materials remains to be studied further.

Declarations

Conflict of interest The authors declare that no competing interests exist.

Ethical approval The research does not require any ethical clearance issue.

References

Afanasyev A, Vedeneeva E (2021) Compositional modeling of multicomponent gas injection into saline aquifers with the MUFITS simulator. J Nat Gas Sci Eng 94:103988

Amaechi CV, Wang F, Ja'e IA, Aboshio A, Odijie AC, Ye J (2022a) A literature review on the technologies of bonded hoses for marine applications. Ships Offshore Struct 17(12):2819–2850

Amaechi CV, Wang F, Ye J (2022b) Experimental study on motion characterisation of CALM buoy hose system under water waves. J Mar Sci Eng 10(2):204

Amaechi CV, Wang F, Ye J (2022c) Understanding the fluid–structure interaction from wave diffraction forces on CALM buoys: numerical and analytical solutions. Ships Offshore Struct 17(11):2545–2573

Andersen T, Skar JI, Hansteen C (1999) Permeability of methane, carbon dioxide and water in PA11 and PVDF Used for flexible pipes. Paper NACE-99410 presented at the CORROSION 99, San Antonio, Texas

Bęben D (2021) The influence of temperature on degradation of oil and gas tubing made of L80-1 steel. Energies 14(20):6855

Benjelloun-Dabaghi Z, de Hemptinne JC, Jarrin J, Leroy JM, Aubry JC, Saas JN, Taravel-Condat C (2002) MOLDI (TM): a fluid permeation model to calculate the annulus composition in flexible pipes. Oil Gas Sci Technol 57(2):177–192

Bertoncello JCB, Simoni L, Tagliari MR, Scheid A, Paes MTP, Kwietniewski CEF (2020) Effects of thermal spray aluminium coating on SSC and HIC resistance of high strength steel in a sour environment. Surf Coat Technol 399:9

Campos T, Gomes JA, Seiersten M, Palencsár S, Dugstad A (2019) Corrosion of armor wire steel in the annulus of flexible pipes at

near neutral pH. Paper NACE-2019-13302 presented at the COR-ROSION 2019, Nashville, Tennessee, USA

Chabab S, Théveneau P, Corvisier J, Coquelet C, Paricaud P, Houriez C, El Ahmar E (2019) Thermodynamic study of the CO_2–H_2O–NaCl system: measurements of CO_2 solubility and modeling of phase equilibria using Soreide and Whitson, electrolyte CPA and SIT models. Int J Greenh Gas Control 91:102825

Clements R, Ethridge AD (2003) Corrosion testing of armour wire in simulated annulus environments of flexible pipelines: an update. In: International conference on offshore mechanics and arctic engineering 2003, vol 36835, pp 339–344. https://doi.org/10.1115/OMAE2003-37473

de Freitas DS, Goncalves IL, Vaz GL (2021) The effect of ethanol added to the natural gas stream on the top of line corrosion: an approach on vapor phase condensation and carbonic acid genera-tion yield. J Nat Gas Sci Eng 96:104297

Eriksen M, Engelbreth KI (2014) Outer cover damages on flexible pipes: corrosion and integrity challenges. In: International con-ference on offshore mechanics and arctic engineering. American Society of Mechanical Engineers, p. V06BT04A016. https://doi.org/10.1115/OMAE2014-24147

Eucken AV (1937) Energie-und stoffaustausch an grenzflächen. Natur-wissenschaften 25:209–218

Haahr M, Gudme J, Sonne J, Overby S, Nielsen T, Rubin A (2016) H_2S consumption and the derivation of a new annulus prediction model for offshore flexible pipes. In: International conference on offshore mechanics and arctic engineering. American Society of Mechanical Engineers, p V005T04A009. https://doi.org/10.1115/OMAE2016-54472

Hu Z, Yue W, Chi H, Xue Z, Tang G, Zhang X (2021) A method to optimize the length of flexible hose of the radial jet drilling technology. J Pet Explor Prod Technol. https://doi.org/10.1007/s13202-021-01381-1

Islam MM, Pojtanabuntoeng T, Gubner R (2018) Corrosion of carbon steel under condensing water and monoethylene glycol. Corros Sci 143:10–22

Jacob M (1936) Heat transfer in evaporation and condensation II. Mech Eng 58:729–740

Khandekar S, Muralidhar K (2014) Dropwise condensation on inclined textured surfaces. Springer, Berlin

Kim S, Kim KJ (2011) Dropwise condensation modeling suitable for superhydrophobic surfaces. ASME J Heat Transf 133(8):081502

Leach RN, Stevens F, Langford SC, Dickinson JT (2006) Drop-wise condensation: experiments and simulations of nuclea-tion and growth of water drops in a cooling system. Langmuir 22(21):8864–8872

Liu Y, Shan L, Guo B, Sun M, Wang G, Wang Q (2020) Numerical solutions of heat transfer problems in gas production from seabed gas hydrates. J Pet Sci Eng 188:106824

Ma XH, Zhou XD, Lan Z, Li YM, Zhang Y (2008) Condensation heat transfer enhancement in the presence of non-condensable gas using the interfacial effect of dropwise condensation. Int J Heat Mass Transf 51(7–8):1728–1737

MacLeod I, Picksley J, Cruickshank K (2017) Sureflex JIP: the latest flexible pipe operational experience and integrity management guidance. In: SPE Offshore Europe conference & exhibition. One-Petro. https://doi.org/10.2118/186158-MS

Matheus FK, Frank PM, Marcelo FB, Thomas GC (2020) RFID wire-less system for detection of water in the annulus of a flexible pipe. Mar Struct 72:102776

Mu CF, Pang JJ, Lu QY, Liu TQ (2008) Effects of surface topography of material on nucleation site density of dropwise condensation. Chem Eng Sci 63(4):874–880

Péneloux A, Rauzy E, Fréze R (1982) A consistent correction for Redlich–Kwong–Soave volumes. Fluid Phase Equilib 8(1):7–23

Qi B, Wei J, Zhang L, Xu H (2015) A fractal dropwise condensation heat transfer model including the effects of contact angle and drop size distribution. Int J Heat Mass Transf 83:259–272

Rausch MH, Froba AP, Leipertz A (2008) Dropwise condensation heat transfer on ion implanted aluminum surfaces. Int J Heat Mass Transf 51(5–6):1061–1070

Rausch MH, Leipertz A, Froba AP (2010) On the characteristics of ion implanted metallic surfaces inducing dropwise condensation of steam. Langmuir 26(8):5971–5975

Remita E, Ropital F, Kittel J, Tribollet B, Sutter E, Condat CT, Desa-mais N (2008) Experimental and theoretical investigation of the uniform corrosion in the annulus of offshore flexible pipelines. Paper NACE-08538 presented at the CORROSION 2008, New Orleans, Louisiana

Rose J (1981) Dropwise condensation theory. Int J Heat Mass Transf 24(2):191–194

Rose J (2002) Dropwise condensation theory and experiment: a review. Proc Inst Mech Eng Part A J Power Energy 216(2):115–128

Rose J, Glicksman L (1973) Dropwise condensation—the distribution of drop sizes. Int J Heat Mass Transf 16(2):411–425

Rozi F, Mohebbi H, Ismail MC, Kakooei S, Ahmadi M, Aghasadeghi A, Aghasadeghi A (2018) Laboratory investigation on the con-densation and corrosion rates of top of line corrosion in carbon steel: a case study from pipeline transporting wet gas in elevated temperature. Corros Eng Sci Technol 53(6):444–448

Song Y, Xu D, Lin J, Tsian S (1991) A study on the mechanism of dropwise condensation. Int J Heat Mass Transf 34(11):2827–2831

Søreide I, Whitson CH (1992) Peng–Robinson predictions for hydro-carbons, CO_2, N_2, and H_2S with pure water and NaCl brine. Fluid Phase Equilib 77:217–240

Taravel-Condat C, Guichard M, Martin J (2003) MOLDI™: a fluid permeation model to calculate the annulus composition in flex-ible pipes—validation with medium scale tests, full scale tests and field cases. In: International conference on offshore mechan-ics and arctic engineering, pp 627–636. https://doi.org/10.1115/OMAE2003-37193

Tsutsumi Y, Nishikata A, Tsuru T (2007) Pitting corrosion mechanism of Type 304 stainless steel under a droplet of chloride solutions. Corros Sci 49(3):1394–1407

Vagapov RK (2021) Comparing and interpreting results of processing in-line inspection data for corrosive gas transportation conditions. Russ J Nondestr Test 57(8):717–726

Wang K, Wang ZM, Song G-L (2020) Batch transportation of oil and water for reducing pipeline corrosion. J Pet Sci Eng 195:107583

Wang K, Yu X, Zheng L, Zhang E, He Y (2021) Numerical investi-gation of gas permeation and condensation behavior of flexible risers. J Pet Sci Eng 203:108622

Wang RG, Kido M (2006) Corrosion behavior of pure iron beneath a micro-droplet of sulfuric acid solution investigated by atomic force microscopy. Scr Mater 55(7):633–636

Wu YT, Yang CX, Yuan XG (2001) Drop distributions and numerical simulation of dropwise condensation heat transfer. Int J Heat Mass Transf 44(23):4455–4464

Zhang L, Xu Z, Lu Z, Du J, Wang EN (2019) Size distribution theory for jumping-droplet condensation. Appl Phys Lett 114(16):163701

Zhang L, Iwata R, Zhao L, Gong S, Lu Z, Xu Z, Zhong Y, Zhu J, Cruz S, Wilke KL (2020a) Nucleation site distribution probed by phase-enhanced environmental scanning electron microscopy. Cell Rep Phys Sci 1(12):100262

Zhang Q, Zhang C, Zhang Z, Zhang N, Liu J (2020b) Galvanic corro-sion behavior of dissimilar casing steels in high sulfur-containing gas wells. Eng Fail Anal 108:104320